Topologically nontrivial and trivial flat bands via weak and strong interlayer coupling in twisted bilayer honeycomb optical lattices for ultracold atoms

Wenjie Sui,[1] Wei Han,[1,2,*] Zheng Vitto Han,[1,2] Zengming Meng,[1,3] and Jing Zhang[1,3,†]
[1]*State Key Laboratory of Quantum Optics Technologies and Devices, Institute of Opto-Electronics, Collaborative Innovation Center of Extreme Optics, Shanxi University, Taiyuan, Shanxi 030006, China*
[2]*Liaoning Academy of Materials, Shenyang 110167, China*
[3]*Hefei National Laboratory, Hefei 230088, China*

(Received 26 February 2025; accepted 13 May 2025; published 6 June 2025)

In recent years, flat electronic bands in twisted bilayer graphene (TBG) have attracted significant attention due to their intriguing topological properties, extremely slow electron velocities, and enhanced density of states. Extending twisted bilayer systems to new configurations is highly desirable, as it offers promising opportunities to explore flat bands beyond TBG. Here, we study both topological and trivial flat bands in a twisted bilayer honeycomb lattice for ultracold atoms and present the evolution of the flat bands with different interlayer coupling strength (ICS). Our results demonstrate that an isolated topological flat band can emerge at the Dirac-point energy for a specific value of weak ICS, referred to as the "critical coupling." This occurs over a wide range of twist angles, surpassing the limits of the magic angle in TBG systems. When the ICS is slightly increased beyond the critical coupling value, the topological flat band exhibits degenerate band crossings with both the upper and lower adjacent bands at the high-symmetry Γ_s point. As the ICS is further increased into the strong coupling regime, trivial flat bands arise around Dirac-point energy. Meanwhile, more trivial flat bands appear, extending from the lowest to higher energy bands, and remain flat as the ICS increases. The topological properties of the flat bands are studied through the winding pattern of the Wilson loop spectrum. Our research provides deeper insights into the formation of flat bands in ultracold atoms with highly controllable twisted bilayer optical lattices, and may contribute to the discovery of new strongly correlated states of matter.

DOI: 10.1103/PhysRevA.111.063306

I. INTRODUCTION

Moiré lattices arise when two similar periodic structures are stacked at a twist angle, resulting in long-period moiré patterns [1–5]. This overlay fundamentally alters the system's original quantum mechanical properties, offering an exciting platform that introduces an additional degree of freedom to manipulate quantum phases, thereby enhancing our understanding of correlated quantum matter [6–10].

In 2018, Cao *et al.* fabricated a graphene moiré lattices by stacking two monolayer graphene sheets with interlayer interactions and tuning the twist angle between them [11,12]. They experimentally demonstrated that a flat band appears near the Fermi level at a special twist angle, referred to as the "magic angle." This flat band leads to a vanishing Fermi velocity at the Dirac point and a high density of states, resulting in the emergence of correlated insulating states and unconventional superconductivity in twisted bilayer graphene (TBG). Since then, graphene-based moiré systems have emerged as a central focus of research, as they offer a clean and versatile platform for studying strongly correlated materials and provide valuable insights into the mechanisms of superconductivity [13–18]. Recently, many exotic phases have been observed in TBG, including the quantum anomalous Hall effect [19,20], the valley Hall effect [20,21], and fractional Chern insulators [22–24]. Theoretical challenges in understanding these correlation-driven phenomena in TBG primarily arise from the presence of flat bands and their associated topological properties [25–28].

Given the limitations on accessible physical parameters, such as the twist angle and interlayer coupling strength, in two-dimensional (2D) materials, extending twisted bilayer van der Waals structures to new platforms is highly desirable, as it offers promising opportunities to explore twistronics beyond TBG. In photonics, moiré lattices have been realized in photonic crystals and photonic lattices, which benefit from highly controllable lattice structures and symmetries [29–31]. These systems have enabled the observation of exotic phenomena such as light localization and high-quality nanocavities [32–34]. In ultracold atoms, a twisted bilayer optical lattice has been realized by our group [35], offering significant advantages for studying moiré physics with unprecedented tunability [36–45].

The moiré flat bands in TBG are critically influenced by both the twist angle and the interlayer coupling strength (ICS). In TBG, the ICS can be finely tuned by applying out-of-plane pressure [17,46–48]. However, the range of this adjustment is quite limited, which poses challenges in studying the continuous transition from weak ICS to strong ICS in moiré physics. Here, based on the highly controllable interlayer coupling of

*Contact author: hanwei.irain@gmail.com
†Contact author: jzhang74@sxu.edu.cn

ultracold atoms in a 2D twisted bilayer honeycomb optical lattice [39], we investigate the rich moiré flat bands across a broad range of twist angles. We identify an isolated topological flat band at the Dirac-point energy for a specific value of weak ICS, referred to as the "critical coupling." The value of this critical coupling depends on the twist angle. When the ICS is slightly increased beyond the critical coupling, the topological flat band touches both the upper and lower bands at the high-symmetry point Γ_s. As the ICS enters the strong coupling regime, multiple trivial flat bands emerge around the Dirac-point energy bands. Here, we define the "Dirac-point energy bands" as the energy bands that form the Dirac point without interlayer coupling. These trivial bands remain flat as the ICS is further increased. We also find that at the critical coupling, the band at the lowest energy becomes flat as well, but it remains a topologically trivial flat band, in contrast to the topologically nontrivial flat band formed at the Dirac-point energy. As the ICS continues to increase, the number of trivial flat bands gradually increases from lower- to higher-energy bands. The topological properties of the flat bands are analyzed by calculating the Wilson loop spectrum.

The rest of the paper is organized as follows. In Sec. II, we present the theoretical model for describing dilute ultracold atomic gases in twisted bilayer honeycomb optical lattices. Specifically, Sec. III A discusses the emergence of topological flat bands in the weak interlayer coupling regime, including the critical coupling as a function of the twist angle. In Sec. III B, we analyze the appearance of trivial flat bands in the strong interlayer coupling regime. Finally, we discuss the experimental relevance of our results and provide concluding remarks in Sec. IV.

II. THEORETICAL MODEL

The twisted bilayer honeycomb optical lattice can be realized using synthetic dimension techniques previously employed in our experiment [35]. Initially, atoms are confined to a quasi-two-dimensional pancake-shaped potential by a deep trap along the z axis. Subsequently, atoms in two different spin states are loaded into two independent honeycomb optical lattices with a relative twist angle. These two lattices selectively address atoms in different spin states, thereby forming a synthetic dimension that represents the bilayer structure. Interlayer coupling is introduced via a microwave field that coherently couples the two spin states.

The Hamiltonian of the system can be written as

$$H = \begin{pmatrix} -\frac{\hbar^2}{2m_a}\nabla^2 + V_1 & \Omega_R \\ \Omega_R & -\frac{\hbar^2}{2m_a}\nabla^2 + V_2 \end{pmatrix}, \tag{1}$$

where m_a is the atomic mass, $\hbar$ is the reduced Planck constant, and Ω_R denotes the ICS. The honeycomb optical lattice potentials V_1 and V_2 are defined as

$$V_1 = V_0\left[\cos\left(\frac{3}{2}k_0x_1 + \frac{\sqrt{3}}{2}k_0y_1\right) + \cos\left(-\frac{3}{2}k_0x_1 + \frac{\sqrt{3}}{2}k_0y_1\right) + \cos(-\sqrt{3}k_0y_1)\right],$$

$$V_2 = V_0\left[\cos\left(\frac{3}{2}k_0x_2 + \frac{\sqrt{3}}{2}k_0y_2\right) + \cos\left(-\frac{3}{2}k_0x_2 + \frac{\sqrt{3}}{2}k_0y_2\right) + \cos(-\sqrt{3}k_0y_2)\right], \tag{2}$$

where the rotated coordinates are defined as $x_1 = x\cos(\theta/2) + y\sin(\theta/2)$, $y_1 = -x\sin(\theta/2) + y\cos(\theta/2)$, $x_2 = x\cos(\theta/2) - y\sin(\theta/2)$, and $y_2 = x\sin(\theta/2) + y\cos(\theta/2)$, with x and y being the spatial coordinates and θ the twist angle. The wave number of the lattice lasers is $k_0 = 2\pi/\lambda$, where λ is the laser wavelength. The lattice depth V_0 is expressed in units of the recoil energy, defined as $E_r = \hbar^2k_0^2/(2m_a)$. The moiré lattice structure formed by V_1 and V_2 is illustrated in Figs. 1(a) and 1(b).

A twisted bilayer honeycomb optical lattice can exhibit either a periodic (commensurate) or an aperiodic (incommensurate) structure, depending on the twist angle. The commensurate twist angles are determined as [49]

$$\theta = \arctan\left(\frac{\sqrt{3}b}{2a+b}\right), \tag{3}$$

where the integers a and b are defined based on the values of m and n, which are coprime natural numbers satisfying $m > n$. If $(m-n)/3$ is an integer, then $a = (m^2-n^2)/3$ and $b = (2mn+n^2)/3$; otherwise, $a = m^2-n^2$ and $b = 2mn+n^2$. Accordingly, the period of the moiré supercell, denoted by λ_{sc}, is given by $\lambda_{sc} = \sqrt{(m^2+n^2+mn)/3} = n\lambda_{mo}$ when $(m-n)/3$ is an integer, and by $\lambda_{sc} = \sqrt{m^2+n^2+mn} = \sqrt{3}n\lambda_{mo}$ when $(m-n)/3$ is a noninteger. Here, $\lambda_{mo} = \lambda/[3\sin(\theta/2)]$ represents the period of the moiré pattern.

The first Brillouin zones of the two honeycomb optical lattices, along with the moiré Brillouin zone defined by the new moiré periodicity, are illustrated in Fig. 1(c). For small twist angles, the moiré Brillouin zone becomes significantly smaller than that of a monolayer honeycomb optical lattice. As a result, each energy band of the monolayer lattice is folded into multiple bands within the moiré Brillouin zone. The number of folded bands is given by $c = (m^2+n^2+mn)/3$ when $(m-n)/3$ is an integer, and by $c = m^2+n^2+mn$ otherwise. For instance, the original s band of the monolayer lattice is folded into the first c bands of the moiré lattice, and the original p band is folded into the moiré bands ranging from $c+1$ to $2c$.

For simplicity, we focus on the case where $n = 1$ and $(m-n)/3$ is an integer, which corresponds to a supercell containing a single period of the moiré pattern, as illustrated in Fig. 1(b). In this scenario, the energy bands exhibit the lowest possible degeneracy. The Dirac point appears within the folded bands, ranging from $2c-1$ to $2c+2$, and we refer to these four bands as the Dirac-point energy bands. Specifically, for $m = 22$, $n = 1$ (corresponding to $\theta \approx 4.4085^\circ$) and $\Omega_R = 0$, the band structure of the twisted bilayer honeycomb optical lattice is shown in Fig. 1(d). As indicated by the red lines, the Dirac-point energy bands are located between the 337th and 340th bands of the moiré lattice. All numerical calculations in this work were performed using the finite element method implemented in COMSOL MULTIPHYSICS.

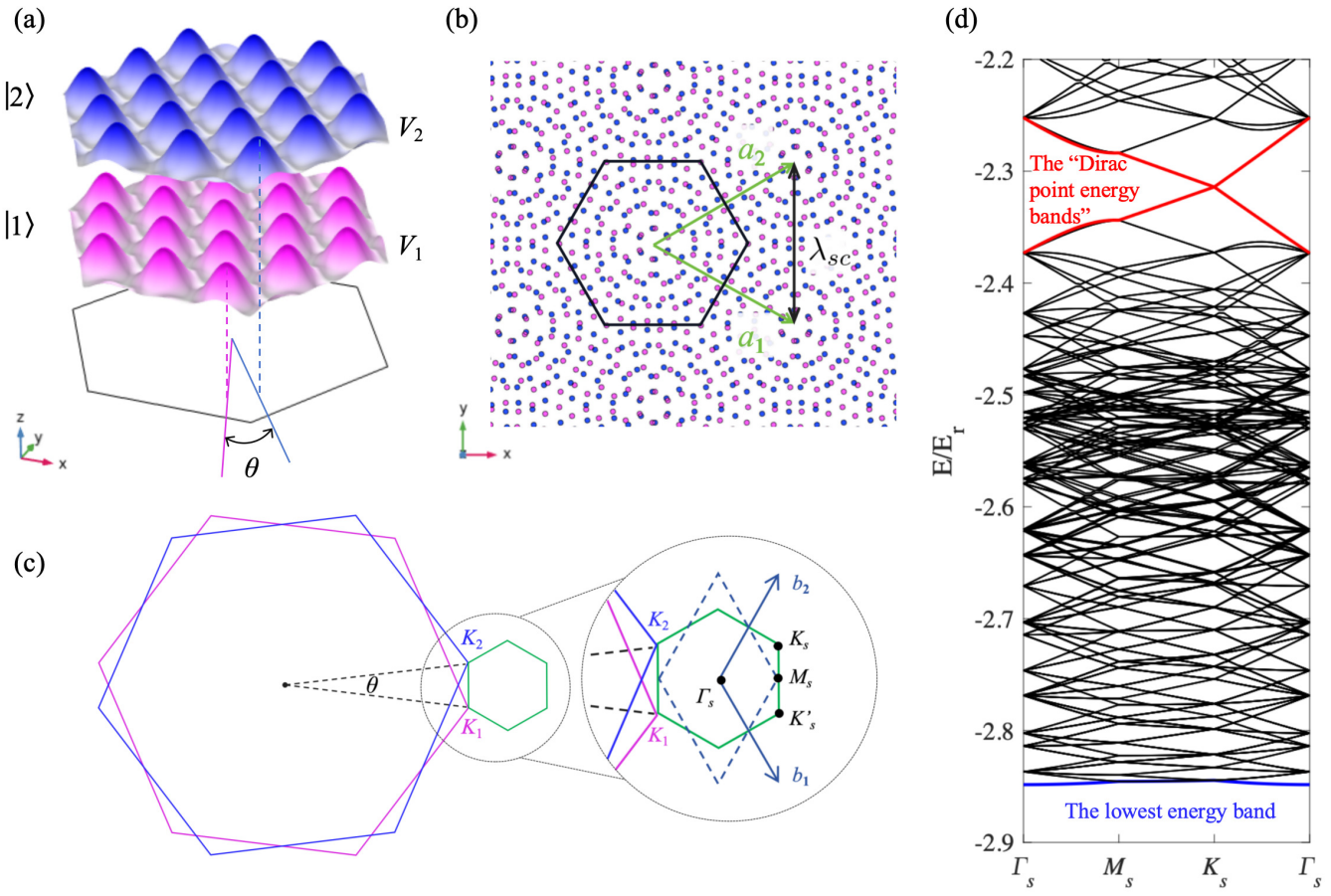

FIG. 1. (a) Moiré supercell formed by two sets of honeycomb optical lattices V_1 (magenta) and V_2 (blue) with a small twist angle θ. The lattices V_1 and V_2 independently confine ultracold atoms in spin states $|1\rangle$ and $|2\rangle$, respectively. (b) Periodic structure of the twisted bilayer honeycomb optical lattice. The magenta and blue dots represent the minima of the optical potentials V_1 and V_2, respectively. $\mathbf{a_1}$ and $\mathbf{a_2}$ denote the lattice vectors, and λ_{sc} is the period of the moiré supercell. (c) The first Brillouin zones of the monolayer honeycomb optical lattices (magenta and blue hexagons), along with the resulting moiré Brillouin zone (green hexagon). The high-symmetry points K_1, K_2, Γ_s, K_s, M_s, and K'_s are labeled, and the reciprocal lattice vectors are denoted by $\mathbf{b_1}$ and $\mathbf{b_2}$. (d) Energy bands of the moiré lattice for $m = 22$, $n = 1$ ($\theta \approx 4.4085^\circ$), with $V_0 = 4E_r$ and $\Omega_R = 0$. The red lines highlight the Dirac-point energy bands, while the blue line indicates the lowest energy band.

III. FLAT BANDS INDUCED BY INTERLAYER COUPLING

The interlayer coupling between atoms in the two twisted optical honeycomb lattices plays a crucial role in determining the energy band structure. We investigate the energy bands in both the weak and strong interlayer coupling regimes, and discuss the emergence of flat bands as well as their topological properties.

A. The weak interlayer coupling regime

We compute the energy band structure for weak ICS near the Dirac point, as shown in Fig. 2. For a fixed commensurable twist angle of $\theta = \arctan\frac{15\sqrt{3}}{337} \approx 4.4085^\circ$, the energy bands and corresponding density of states for different ICS values are presented in Figs. 2(a)–2(d). Compared with the zero ICS case shown in Fig. 1(d), one can clearly see from Fig. 2(a) that the interlayer coupling significantly reduces the energy width of the Dirac cone and opens two band gaps between the Dirac-point energy bands and their adjacent upper and lower bands. The continued existence of the Dirac point, along with the emergence of band gaps between the Dirac-point energy bands and their adjacent bands, can be understood as follows: The Dirac point degeneracy originates from the sublattice symmetry between the A and B sites in a single-layer honeycomb lattice. This type of degeneracy is protected by both time-reversal symmetry and spatial inversion symmetry (sublattice exchange). In the regime of weak interlayer coupling, the Dirac points in the bilayer system remain largely governed by the intrinsic sublattice symmetry of each individual layer, thus the interlayer coupling is insufficient to break this symmetry-protected degeneracy. In contrast, the degenerate crossings between the Dirac-point energy bands and their adjacent bands arise from the band folding in momentum space of single-layer graphene energy bands into the mini Brillouin zone of the moiré superlattice. These degeneracies are purely geometric and accidental, not protected by symmetry. Such accidental degeneracies are generally lifted by even weak interlayer coupling.

As the ICS approaches a critical value, the group velocity at the Dirac point nearly vanishes, the hybridized energy bands become flat, and a pronounced peak emerges in the density of states, as shown in Fig. 2(b). This specific value of ICS, which minimizes the bandwidth, is referred to as the

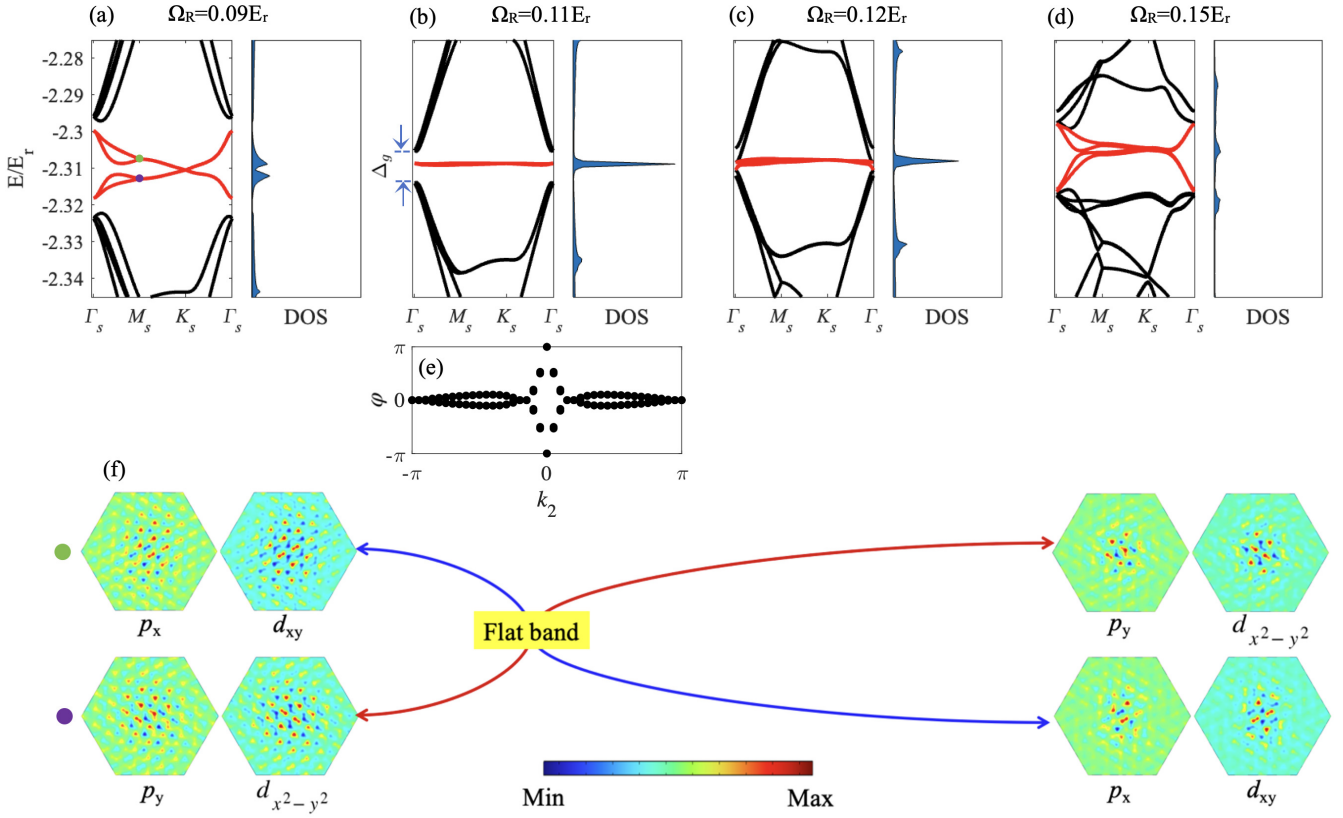

FIG. 2. (a)–(d) Energy bands and corresponding density of states near the Dirac points of the twisted bilayer honeycomb optical lattice for increasing interlayer coupling strength $\Omega_R = 0.09E_r$, $0.11E_r$, $0.12E_r$, and $0.15E_r$, respectively. (e) Wilson loop of the topological flat band shown in (b). (f) Real part of the eigenstates at the M_s point of the moiré Brillouin zone for interlayer coupling strength $\Omega_R = 0.09E_r$ (left panel) and $0.15E_r$ (right panel). The twist angle is fixed at $\theta \approx 4.4085^\circ$, and the lattice depth is set to $V_0 = 4E_r$.

critical coupling. When the ICS is slightly increased beyond the critical coupling, the flat band touches the upper and lower bands at the high-symmetry Γ_s point, as shown in Fig. 2(c). In this regime, the previously isolated flat band evolves into a singular flat band with band touching. Upon further increasing the ICS, the bandwidth broadens and the flatness of the band is lost, as illustrated in Fig. 2(d).

To gain deeper insight into the formation of the flat band, we analyze the energies and Bloch modes of the Dirac-point energy bands at the M_s point of the moiré Brillouin zone, which is associated with Van Hove singularities [11]. As shown in Figs. 2(a)–2(d), interlayer coupling induces energy splitting at the M_s point, bringing the energies of the four Bloch modes from the Dirac-point energy bands closer to that of the Dirac point. As the ICS increases to the critical coupling, these four Bloch modes become degenerate with the Dirac-point energy, resulting in the formation of flat bands. When the ICS increases further, the energies of the four Bloch modes split again, lifting the degeneracy and resulting in the disappearance of the flat band. Meanwhile, we observe an orbital exchange among the Bloch modes of the Dirac-point energy bands before and after the band flattens, as illustrated in Fig. 2(f). Before the band becomes flat, the upper two bands host Bloch modes with p_x-like and d_{xy}-like orbitals, while the lower two bands contain p_y-like and $d_{x^2-y^2}$-like orbitals. After the flat band disappears due to increased ICS, this orbital distribution is reversed: the upper two bands exhibit p_y-like and $d_{x^2-y^2}$-like orbitals, while the lower two bands exhibit p_x-like and d_{xy}-like orbitals.

The topological properties of the flat bands can be characterized by examining the Wilson loop spectrum [26]. According to the formalism developed by Wilczek and Zee [50], the time evolution of quantum states in an adiabatic system is described by the following path-ordered integral:

$$\hat{W}_{\mathbf{k}(0)\to\mathbf{k}(t)} = \mathcal{P}\exp\left[i\oint_C \hat{A}(\mathbf{k})\cdot d\mathbf{k}\right], \tag{4}$$

where $\mathcal{P}$ denotes path ordering, and the integration path C extends from $\mathbf{k}(0)$ to $\mathbf{k}(t)$ in reciprocal space. Here, $\hat{A}(\mathbf{k})$ is the non-Abelian Berry connection, which captures the local geometric properties of the state space. In a periodic system, the Bloch state for the nth band at a wave vector $\mathbf{k}$ is given by $|\psi_{n,\mathbf{k}}(\mathbf{r})\rangle = e^{i\mathbf{k}\cdot\mathbf{r}}|u_{n,\mathbf{k}}\rangle$. The matrix elements of the non-Abelian Berry connection are determined by the periodic part of the wave function $|u_{n,\mathbf{k}}\rangle$, and are calculated as $[A(\mathbf{k})]_{nn'} = i\langle u_{n,\mathbf{k}}|\nabla_{\mathbf{k}}|u_{n',\mathbf{k}}\rangle$.

We parametrize the wave vector as $\mathbf{k} = \frac{k_1}{2\pi}\mathbf{b_1} + \frac{k_2}{2\pi}\mathbf{b_2}$ in the rhombus-shaped moiré Brillouin zone, where $\mathbf{b_1}$ and $\mathbf{b_2}$ are the reciprocal lattice vectors, as shown in Fig. 1(c). For calculating the Wilson loop, we choose a path with a fixed k_2 in the moiré Brillouin zone, which is parallel to the $\mathbf{b_1}$ direction. In the case of an isolated energy band, the Wilson

loop can be computed as

$$W_{k_2} = \prod_{i=1}^{j} \langle u_{n,k_1^i,k_2} | u_{n,k_1^{i+1},k_2} \rangle, \tag{5}$$

where j is sufficiently large to describe the infinite lattice limit $j \to \infty$. The Berry phase for characterizing the topological property of a single band is then given by

$$\varphi_{k_2} = \mathrm{Im}\big[\ln(W_{k_2})\big]. \tag{6}$$

For N degenerate bands, the Wilson loop matrix can be calculated as

$$\hat{W}_{k_2} = \prod_{i=1}^{j} \hat{M}^{(k_1^i,k_2),(k_1^{i+1},k_2)}, \tag{7}$$

where $\hat{M}$ is a $N \times N$ matrix, and its matrix elements are given by

$$M_{nn'}^{(k_1^i,k_2),(k_1^{i+1},k_2)} = \langle u_{n,k_1^i,k_2} | u_{n',k_1^{i+1},k_2} \rangle, \tag{8}$$

with $n, n' \in \{1, \ldots, N\}$. Then, the Berry phases, which characterize the topological properties of multiple bands, are obtained from the eigenvalues of the Wilson loop matrix as

$$\varphi_{k_2}^n = \mathrm{Im}\big[\ln\big(w_{k_2}^n\big)\big], \tag{9}$$

where $w_{k_2}^n$ is the nth eigenvalue of the matrix $\hat{W}_{k_2}$.

It is worth noting that the Berry phase is related to the Wannier center c [51], which represents the centroid of the maximally localized Wannier function [52]. When $c = \pm 0.5$, the centroid of the maximally localized Wannier function lies at the edge of the primitive cell, whereas for $c = 0$, it is located at the center of the primitive cell. In general, the Wannier function is obtained by performing a Fourier transform of the Bloch function over the two-dimensional Brillouin zone. Here, we get the Wannier function by applying a Fourier transform only along the k_1 direction for a fixed k_2. As a result, the Wannier center c becomes a function of k_2, and is related to the Berry phase by $c(k_2) = \varphi(k_2)/2\pi$. The evolution of the Wannier center with respect to k_2 directly reflects the topological properties of the band. For a topologically nontrivial band, the Wannier center is delocalized, and the Berry phase spans the full range of $[-\pi, \pi]$. In contrast, for a topologically trivial band, the Wannier center is localized, corresponding to a localized spectrum of the Berry phase.

For the flat band shown in Fig. 2(b), the Wilson loop is calculated and presented in Fig. 2(e). It is evident that the Wilson loop, characterized by a winding number $w = 1$, spans the entire moiré Brillouin zone, indicating the nontrivial topology of the flat band. Previous studies have shown that topological flat bands originating from Dirac-point energy bands in twisted bilayer systems exhibit a distinct type of topology known as fragile topology [26,53]. Fragile topological phases typically do not feature gapless edge states, thereby violating the conventional bulk-boundary correspondence, and hold great potential for modeling and engineering unconventional correlated materials [54,55].

To illustrate the influence of the twist angle and ICS on the bandwidth in detail, we calculate the bandwidth ΔE as a function of Ω_R for various twist angles θ. As shown in Fig. 3(a), for a fixed twist angle, the bandwidth significantly decreases with increasing ICS, reaching a minimum at a critical coupling strength. This indicates that even for relatively large twist angles (e.g., $\theta \approx 5.0858^\circ$ with $m = 19$), the topological band near the Dirac point can still be effectively flattened. This provides a more flexible approach to realizing topological flat bands, in contrast to the narrow magic angle range ($\sim 1^\circ$) required in twisted bilayer graphene. Moreover, Fig. 3(a) shows that as the twist angle increases, a larger critical coupling strength is required to flatten the topological band. When the twist angle $\theta \gtrsim 7.341^\circ$ ($m \leqslant 13$), the critical coupling is no longer sufficient to induce flat bands, as demonstrated in Fig. 3(b). We further compute the relative bandwidth $\Delta E/\Delta_g$ at the critical coupling for different twist angles, where $\Delta_g/2$ denotes the average band gap between the flat band and its neighboring upper or lower band, as shown in Fig. 3(c). It is evident that for $\theta \lesssim 6.009^\circ$ ($m \geqslant 16$), the relative bandwidth remains small ($\Delta E/\Delta_g < 0.2$), whereas for $\theta \gtrsim 7.341^\circ$ ($m \leqslant 13$), the relative bandwidth becomes large ($\Delta E/\Delta_g > 0.5$). In addition, we investigate the dependence of the critical coupling strength on the lattice depth V_0, and find that increasing V_0 reduces the critical coupling strength required for the emergence of topological flat bands. The corresponding critical coupling strengths for various twist angles θ and lattice depths V_0 are summarized in Table I.

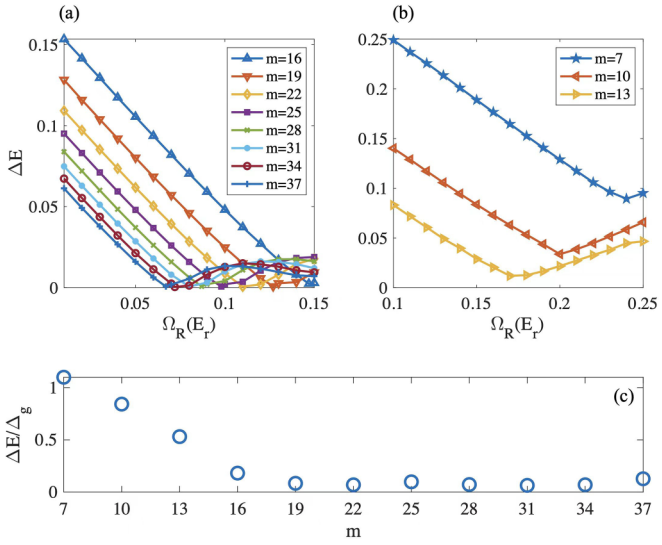

FIG. 3. The bandwidth of the Dirac-point energy bands as a function of the interlayer coupling strength for various twist angles. (a) The cases with $n = 1$, $m = 16$, 19, 22, 25, 28, 31, 34, and 37, corresponding to twist angles $\theta \approx 6.009^\circ$, 5.0858°, 4.4085°, 3.8902°, 3.481°, 3.1497°, 2.8759°, and 2.6459°. (b) The cases with $n = 1, m = 7$, 10, and 13, corresponding to $\theta \approx 13.174^\circ$, 9.43°, and 7.341°. (c) The relative bandwidth $\Delta E/\Delta_g$ at the critical coupling as a function of twist angle. The lattice depth is fixed at $V_0 = 4E_r$ throughout.

B. The strong interlayer coupling regime

As discussed above, when the ICS increases further, the topological flat bands around the Dirac point gradually lose

TABLE I. Critical coupling strengths for different twist angles. The twist angles θ are derived from commensurate configurations with $n = 1$ and $(m - n)/3$ being an integer. $\Omega_R^a(E_r)$ and $\Omega_R^b(E_r)$ denote the critical coupling strengths for lattice depths $V_0 = 4E_r$ and $6E_r$, respectively.

m	θ (deg)	$\Omega_R^a\ (E_r)$	$\Omega_R^b\ (E_r)$
19	5.0858	0.127	0.115
22	4.4085	0.110	0.101
25	3.8902	0.098	0.089
28	3.4810	0.087	0.080
31	3.1497	0.079	0.072
34	2.8759	0.072	0.066
37	2.6459	0.067	0.061
40	2.4500	0.062	0.056
43	2.2811	0.058	0.052
46	2.1339	0.054	0.049
49	2.0046	0.050	0.046

their flatness. In contrast, the lowest-energy bands behave quite differently. At the critical coupling, the lowest band becomes an isolated and nearly flat single band, as exemplified by $\theta \approx 4.4085^\circ$ ($m = 22$), as shown in Fig. 4(a). As the ICS continues to increase, this lowest-energy band becomes increasingly flat, as illustrated in Fig. 4(b). Furthermore, an increasing number of flat bands emerge sequentially from lower to higher energies and remain flat with increasing ICS, as shown in Figs. 4(b) and 4(c). The detailed evolution of the bandwidth ΔE for the lowest ten bands as a function of ICS is shown in Fig. 4(d).

The emergence of flat bands results in real-space localization of the corresponding eigenstates. The real parts of the eigenstates associated with the lowest ten energy bands are displayed in the insets of Fig. 4(c). Specifically, the first, the degenerate second and third, the fourth, the degenerate fifth and sixth, the degenerate seventh and eighth, the ninth, and the tenth bands are composed of localized orbitals resembling $1s$, $2p_x$ ($2p_y$), $2s$, $3p_x$ ($3p_y$), $3d_{xy}$ ($3d_{x^2-y^2}$), $4f_{x(x^2-3y^2)}$, and $4f_{y(3x^2-y^2)}$ orbitals, respectively. It is worth noting that although the ninth and tenth bands are nearly degenerate, they can still be regarded as two isolated bands. For a given flat band, we find that the periodic part of the Bloch eigenstates is independent of the wave vector. This implies a vanishing quantum metric and Berry curvature, indicating a topologically trivial band structure. By calculating the Wilson loop, we have verified that all of the lowest ten flat bands are topologically trivial, as shown in Fig. 4(e).

Further increasing the ICS into the strong coupling regime leads to the emergence of additional flat bands at higher energies. Notably, for sufficiently strong ICS, the Dirac-point energy bands become flat once again. In Figs. 5(a)–5(c), we display the 337th–340th bands along with their nearby bands at $\Omega_R = 2E_r$, $6E_r$, and $10E_r$, respectively. The 337th–340th energy bands, highlighted in red, correspond to the Dirac-point energy bands at $m = 22$. It is evident that flat bands reappear near the Dirac point when Ω_R exceeds $6E_r$. In contrast to the topologically nontrivial flat bands that emerge near the Dirac point at the critical coupling, the flat bands formed in the strong interlayer coupling regime are all topologically trivial. This is confirmed by calculating the Wilson loops, as shown in Figs. 5(d)–5(f). As the ICS approaches infinity, the system effectively reduces to a single layer (or single component) subjected to a twisted optical lattice [35], which has been studied experimentally in photonic systems [32,34,56–58].

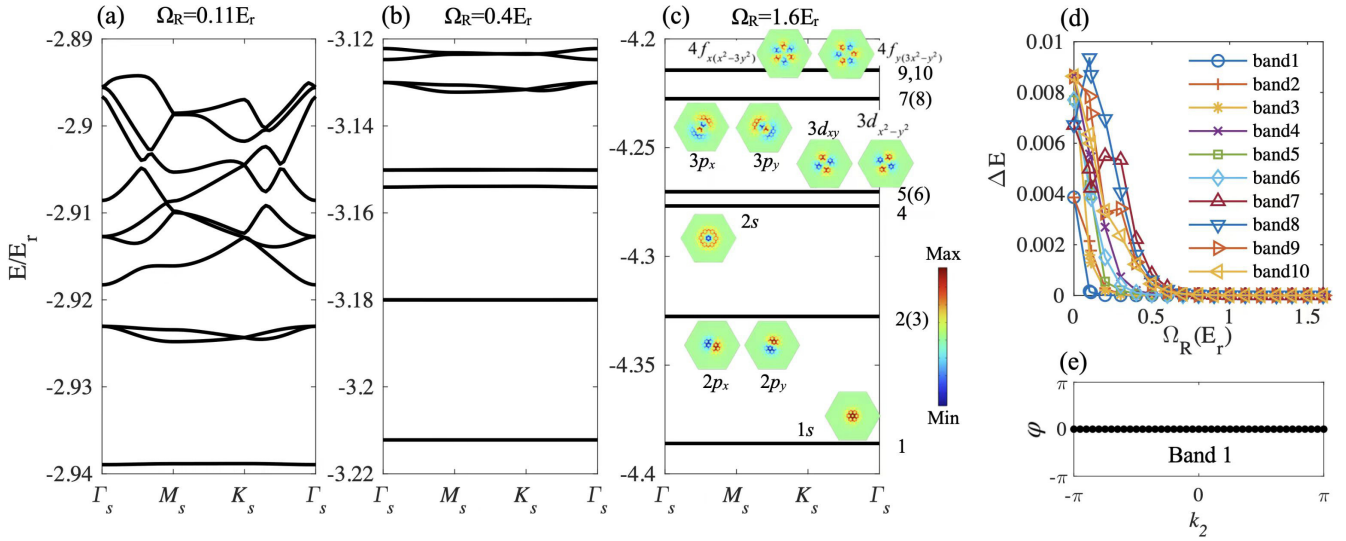

FIG. 4. Trivial flat bands emerging within the lowest ten energy bands in the strong interlayer coupling regime. (a)–(c) The lowest ten energy bands for $n = 1$, $m = 22$ (corresponding to $\theta \approx 4.4085^\circ$), with $\Omega_R = 0.11E_r$, $0.4E_r$, and $1.6E_r$, respectively. Insets in (c) show the real parts of the eigenstates for the lowest ten bands. Specifically, the first, degenerate second (third), fourth, degenerate fifth (sixth), degenerate seventh (eighth), ninth, and tenth bands correspond to localized orbitals resembling $1s$, $2p_x/2p_y$, $2s$, $3p_x/3p_y$, $3d_{xy}/3d_{x^2-y^2}$, $4f_{x(x^2-3y^2)}$, and $4f_{y(3x^2-y^2)}$, respectively. (d) Evolution of the bandwidth ΔE of the lowest ten bands as a function of the interlayer coupling strength Ω_R. (e) Wilson loop of the lowest band with trivial topology.

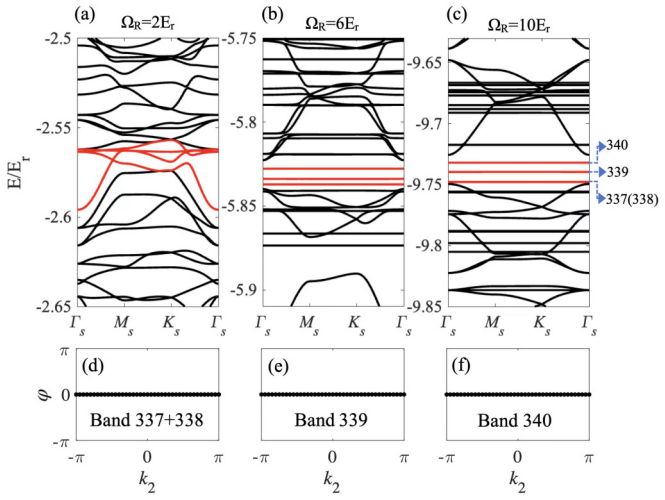

FIG. 5. Trivial flat bands formed by the Dirac-point energy bands in the strong interlayer coupling regime. (a)–(c) The Dirac-point energy bands (337th–340th bands for $m = 22$) highlighted in red, along with nearby energy bands, for $\Omega_R = 2E_r, 6E_r$, and $10E_r$, respectively. (d)–(f) Wilson loops of the trivial flat bands.

IV. DISCUSSION AND CONCLUSION

In realistic experiments, the topological and trivial flat bands can be detected by employing amplitude modulation spectroscopy [59,60] and spin-injection radio-frequency spectroscopy [61–63], which can induce interband transitions and allow for the reconstruction of the band dispersion. To observe the topological properties of flat bands near the Dirac point, atoms can be transported through reciprocal space by uniformly accelerating the lattice via a linear frequency sweep of the lattice beams [64,65]. This generates a constant inertial force, enabling access to the Wilson line regime, where the dynamics are governed entirely by geometric effects. The Wilson line can then be measured by tracking changes in the band populations [66].

One can use the clock states $^1S_0$ and $^3P_0$ of alkaline-earth(-like) atoms as the two pseudospin states for the twisted bilayer optical lattices [39,67]. The $J = 0 \rightarrow J = 0$ forbidden transitions result in an extremely narrow natural linewidth (approximately 1 mHz), and the transition is insensitive to magnetic field perturbations, making it beneficial for the high-precision detection of the energy bands. Considering the ultranarrow gap between the topological flat band and neighboring bands, which may exceed the atomic thermal energy at finite temperature, experimental detection becomes challenging. A promising solution is to enhance the gap by introducing spatially dependent interlayer coupling [5,68].

While the topological flat band at the single-particle level is similar to that in twisted bilayer graphene, the strongly correlated effects induced by the flat band in ultracold atoms will be fundamentally different from those in graphene. This is attributed to the unique and highly tailorable many-body interactions in ultracold atomic systems [69–71]. For example, the attractive s-wave interaction between the Fermi atoms from different layers may induce a Larkin-Ovchinnikov superfluid at the topological flat bands [39]. This phase exhibits a nonzero pairing momentum and a staggered superfluid density distribution in real space, and can be experimentally observed through time-of-flight measurements and *in situ* imaging. In addition, exotic Mott insulating phases or Bose glass phases may also emerge due to the interplay between the flat bands and the interlayer atomic interactions [72].

In summary, we have studied the energy bands of twisted bilayer honeycomb optical lattices for ultracold atoms, with highly controllable interlayer coupling. We find that topologically nontrivial flat bands can form at a critical coupling in the weak interlayer coupling regime, whereas topologically trivial flat bands emerge in the strong interlayer coupling regime. With increasing interlayer coupling strength, the topologically nontrivial flat bands lose their flatness, whereas the topologically trivial flat bands become progressively flatter. For large twist angles, topological flat bands around the Dirac point can also be formed by tuning the interlayer coupling strength. This goes beyond the limitations of the twist angle in twisted bilayer graphene. Our research reveals the physical principles of moiré bands more deeply and provides a universal guideline for applying moiré bands in other fields, including optics, acoustics, and condensed matter.

ACKNOWLEDGMENTS

This research is supported by the National Key Research and Development Program of China (Grants No. 2022YFA1404101 and No. 2021YFA1401700), the Innovation Program for Quantum Science and Technology (Grant No. 2021ZD0302003), and the National Natural Science Foundation of China (Grants No. 12488301, No. 12034011, No. U23A6004, No. 12474266, No. 12474252, No. 12374245, No. 12322409, and No. 92065108).

DATA AVAILABILITY

The data that support the findings of this article are not publicly available. The data are available from the authors upon reasonable request.

[1] P. C. Adak, S. Sinha, U. Ghorai, L. D. V. Sangani, K. Watanabe, T. Taniguchi, R. Sensarma, and M. M. Deshmukh, Tunable bandwidths and gaps in twisted double bilayer graphene on the verge of correlations, Phys. Rev. B **101**, 125428 (2020).

[2] L. Huang, W. Zhang, and X. Zhang, Moiré quasibound states in the continuum, Phys. Rev. Lett. **128**, 253901 (2022).

[3] E. Khalaf, A. J. Kruchkov, G. Tarnopolsky, and A. Vishwanath, Magic angle hierarchy in twisted graphene multilayers, Phys. Rev. B **100**, 085109 (2019).

[4] M. Liang, M.-M. Xiao, Z. Ma, and J.-H. Gao, Moiré band structures of the double twisted few-layer graphene, Phys. Rev. B **105**, 195422 (2022).

[5] G. Tarnopolsky, A. J. Kruchkov, and A. Vishwanath, Origin of magic angles in twisted bilayer graphene, Phys. Rev. Lett. **122**, 106405 (2019).

[6] S. Zhang, R. Xu, N. Luo, and X. Zou, Two-dimensional magnetic materials: structures, properties and external controls, Nanoscale **13**, 1398 (2021).

[7] D. M. Kennes, L. Xian, M. Claassen, and A. Rubio, One-dimensional flat bands in twisted bilayer germanium selenide, Nat. Commun. **11**, 1124 (2020).

[8] X. Lu *et al.*, Superconductors, orbital magnets and correlated states in magic-angle bilayer graphene, Nature (London) **574**, 653 (2019).

[9] J. Wang, X. Mu, L. Wang, and M. Sun, Properties and applications of new superlattice: twisted bilayer graphene, Mater. Today Phys. **9**, 100099 (2019).

[10] D. M. Kennes *et al.*, Moiré heterostructures as a condensed-matter quantum simulator, Nat. Phys. **17**, 155 (2021).

[11] Y. Cao, V. Fatemi, A. Demir, S. Fang, S. L. Tomarken, J. Y. Luo, J. D. Sanchez-Yamagishi, K. Watanabe, T. Taniguchi, E. Kaxiras, R. C. Ashoori, and P. Jarillo-Herrero, Correlated insulator behaviour at half-filling in magic-angle graphene superlattices, Nature (London) **556**, 80 (2018).

[12] Y. Cao, V. Fatemi, S. Fang, K. Watanabe, T. Taniguchi, E. Kaxiras, and P. Jarillo-Herrero, Unconventional superconductivity in magic-angle graphene superlattices, Nature (London) **556**, 43 (2018).

[13] C. C. Liu, L. D. Zhang, W. Q. Chen, and F. Yang, Chiral spin density wave and *d+id* superconductivity in the magic-angle-twisted bilayer graphene, Phys. Rev. Lett. **121**, 217001 (2018).

[14] C. Xu and L. Balents, Topological superconductivity in twisted multilayer graphene, Phys. Rev. Lett. **121**, 087001 (2018).

[15] J. Gonzalez and T. Stauber, Kohn-Luttinger superconductivity in twisted bilayer graphene, Phys. Rev. Lett. **122**, 026801 (2019).

[16] B. Lian, Z. Wang, and B. A. Bernevig, Twisted bilayer graphene: A phonon-driven superconductor, Phys. Rev. Lett. **122**, 257002 (2019).

[17] M. Yankowitz *et al.*, Tuning superconductivity in twisted bilayer graphene, Science **363**, 1059 (2019).

[18] L. Balents, C. R. Dean, D. K. Efetov, and A. F. Young, Superconductivity and strong correlations in moiré flat bands, Nat. Phys. **16**, 725 (2020).

[19] F. Wu, T. Lovorn, E. Tutuc, and A. H. MacDonald, Hubbard model physics in transition metal dichalcogenide moiré bands, Phys. Rev. Lett. **121**, 026402 (2018).

[20] N. Bultinck, S. Chatterjee, and M. P. Zaletel, Mechanism for anomalous Hall ferromagnetism in twisted bilayer graphene, Phys. Rev. Lett. **124**, 166601 (2020).

[21] J. Liu, Z. Ma, J. Gao, and X. Dai, Quantum valley Hall effect, orbital magnetism, and anomalous Hall effect in twisted multilayer graphene systems, Phys. Rev. X **9**, 031021 (2019).

[22] Y. Xie *et al.*, Fractional Chern insulators in magic-angle twisted bilayer graphene, Nature (London) **600**, 439 (2021).

[23] V. Crépel and L. Fu, Anomalous Hall metal and fractional Chern insulator in twisted transition metal dichalcogenides, Phys. Rev. B **107**, L201109 (2023).

[24] C. Repellin and T. Senthil, Chern bands of twisted bilayer graphene: Fractional Chern insulators and spin phase transition, Phys. Rev. Res. **2**, 023238 (2020).

[25] H. C. Po, H. Watanabe, and A. Vishwanath, Fragile topology and Wannier obstructions, Phys. Rev. Lett. **121**, 126402 (2018).

[26] Z. Song, Z. Wang, W. Shi, G. Li, C. Fang, and B. A. Bernevig, All magic angles in twisted bilayer graphene are topological, Phys. Rev. Lett. **123**, 036401 (2019).

[27] J. Ahn, S. Park, and B.-J. Yang, Failure of Nielsen-Ninomiya theorem and fragile topology in two-dimensional systems with space-time inversion symmetry: Application to twisted bilayer graphene at magic angle, Phys. Rev. X **9**, 021013 (2019).

[28] J.-T. Wang, J.-X. Liu, H.-T. Ding, and P. He, Proposal for implementing Stiefel-Whitney insulators in an optical Raman lattice, Phys. Rev. A **109**, 053314 (2024).

[29] K. Dong, T. Zhang, J. Li, Q. Wang, F. Yang, Y. Rho, D. Wang, C. P. Grigoropoulos, J. Wu, and J. Yao, Flat bands in magic-angle bilayer photonic crystals at small twists, Phys. Rev. Lett. **126**, 223601 (2021).

[30] B. Lou, N. Zhao, M. Minkov, C. Guo, M. Orenstein, and S. Fan, Theory for twisted bilayer photonic crystal slabs, Phys. Rev. Lett. **126**, 136101 (2021).

[31] C. H. Yi, H. C. Park, and M. J. Park, Strong interlayer coupling and stable topological flat bands in twisted bilayer photonic Moiré superlattices, Light Sci. Appl. **11**, 289 (2022).

[32] P. Wang, Y. Zheng, X. Chen, C. Huang, Y. V. Kartashov, L. Torner, V. V. Konotop, and F. Ye, Localization and delocalization of light in photonic moiré lattices, Nature (London) **577**, 42 (2020).

[33] H. Tang, F. Du, S. Carr, C. DeVault, O. Mello, and E. Mazur, Modeling the optical properties of twisted bilayer photonic crystals, Light Sci. Appl. **10**, 157 (2021).

[34] X. R. Mao, Z. K. Shao, H. Y. Luan, S. L. Wang, and R. M. Ma, Magic-angle lasers in nanostructured moiré superlattice, Nat. Nanotechnol. **16**, 1099 (2021).

[35] Z. Meng, L. Wang, W. Han, F. Liu, K. Wen, C. Gao, P. Wang, C. Chin, and J. Zhang, Atomic Bose-Einstein condensate in twisted-bilayer optical lattices, Nature (London) **615**, 231 (2023).

[36] M. McDonald, J. Trisnadi, K.-X. Yao, and C. Chin, Superresolution microscopy of cold atoms in an optical lattice, Phys. Rev. X **9**, 021001 (2019).

[37] A. González-Tudela and J. I. Cirac, Cold atoms in twisted-bilayer optical potentials, Phys. Rev. A **100**, 053604 (2019).

[38] T. Salamon, A. Celi, R. W. Chhajlany, I. Frérot, M. Lewenstein, L. Tarruell, and D. Rakshit, Simulating twistronics without a twist, Phys. Rev. Lett. **125**, 030504 (2020).

[39] X.-W. Luo and C. Zhang, Spin-twisted optical lattices: tunable flat bands and Larkin-Ovchinnikov superfluids, Phys. Rev. Lett. **126**, 103201 (2021).

[40] C. Wang, C. Gao, J. Zhang, H. Zhai, and Z.-Y. Shi, Three-dimensional moiré crystal in ultracold atomic gases, Phys. Rev. Lett. **133**, 163401 (2024).

[41] M. Gall, N. Wurz, J. Samland, C. F. Chan, and M. Köhl, Competing magnetic orders in a bilayer Hubbard model with ultracold atoms, Nature (London) **589**, 40 (2021).

[42] L. Tarruell, D. Greif, T. Uehlinger, G. Jotzu, and T. Esslinger, Creating, moving and merging Dirac points with a Fermi gas in a tunable honeycomb lattice, Nature (London) **483**, 302 (2012).

[43] P. Soltan-Panahi, J. Struck, P. Hauke, A. Bick, W. Plenkers, G. Meineke, C. Becker, P. Windpassinger, M. Lewenstein, and K. Sengstock, Multi-component quantum gases in spin-dependent hexagonal lattices, Nat. Phys. **7**, 434 (2011).

[44] P. Windpassinger and K. Sengstock, Engineering novel optical lattices, Rep. Prog. Phys. **76**, 086401 (2013).
[45] I. Bloch, J. Dalibard, and W. Zwerger, Many-body physics with ultracold gases, Rev. Mod. Phys. **80**, 885 (2008).
[46] S. Carr, S. Fang, P. Jarillo-Herrero, and E. Kaxiras, Pressure dependence of the magic twist angle in graphene superlattices, Phys. Rev. B **98**, 085144 (2018).
[47] B. L. Chittari, N. Leconte, S. Javvaji, and J. Jung, Pressure induced compression of flatbands in twisted bilayer graphene, Electron. Struct. **1**, 015001 (2018).
[48] M. Yankowitz, J. Jung, E. Laksono, N. Leconte, B. L. Chittari, K. Watanabe, T. Taniguchi, S. Adam, D. Graf, and C. R. Dean, Dynamic band-structure tuning of graphene moiré superlattices with pressure, Nature (London) **557**, 404 (2018).
[49] J. M. B. Lopes dos Santos, N. M. R. Peres, and A. H. C. Neto, Graphene bilayer with a twist: Electronic structure, Phys. Rev. Lett. **99**, 256802 (2007).
[50] F. Wilczek and A. Zee, Appearance of gauge structure in simple dynamical systems, Phys. Rev. Lett. **52**, 2111 (1984).
[51] M. Taherinejad, K. F. Garrity, and D. Vanderbilt, Wannier center sheets in topological insulators, Phys. Rev. B **89**, 115102 (2014).
[52] N. Marzari and D. Vanderbilt, Maximally localized generalized Wannier functions for composite energy bands, Phys. Rev. B **56**, 12847 (1997).
[53] H. C. Po, L. Zou, T. Senthil, and A. Vishwanath, Faithful tight-binding models and fragile topology of magic-angle bilayer graphene, Phys. Rev. B **99**, 195455 (2019).
[54] Z.-D. Song, L. Elcoro, and B. A. Bernevig, Twisted bulk-boundary correspondence of fragile topology, Science **367**, 794 (2020).
[55] V. Peri, Z.-D. Song, M. Serra-Garcia, P. Engeler, R. Queiroz, X. Huang, W. Deng, Z. Liu, B. A. Bernevig, and S. D. Huber, Experimental characterization of fragile topology in an acoustic metamaterial, Science **367**, 797 (2020).
[56] Q. Fu, P. Wang, C. Huang, Y. V. Kartashov, L. Torner, V. V. Konotop, and F. Ye, Optical soliton formation controlled by angle twisting in photonic moiré lattices, Nat. Photon. **14**, 663 (2020).
[57] C. Huang, F. Ye, X. Chen, Y. V. Kartashov, V. V. Konotop, and L. Torner, Localization-delocalization wavepacket transition in Pythagorean aperiodic potentials, Sci. Rep. **6**, 32546 (2016).
[58] H.-Y. Luan, Y.-H. Ouyang, Z.-W. Zhao, W.-Z. Mao, and R.-M. Ma, Reconfigurable moiré nanolaser arrays with phase synchronization, Nature (London) **624**, 282 (2023).
[59] T. Stöferle, H. Moritz, C. Schori, M. Köhl, and T. Esslinger, Transition from a strongly interacting 1D superfluid to a Mott insulator, Phys. Rev. Lett. **92**, 130403 (2004).
[60] N. Fläschner, M. Tarnowski, B. S. Rem, D. Vogel, K. Sengstock, and C. Weitenberg, High-precision multiband spectroscopy of ultracold fermions in a nonseparable optical lattice, Phys. Rev. A **97**, 051601(R) (2018).
[61] J. T. Stewart, J. P. Gaebler, and D. S. Jin, Using photoemission spectroscopy to probe a strongly interacting Fermi gas, Nature (London) **454**, 744 (2008).
[62] P. Wang, Z.-Q. Yu, Z. Fu, J. Miao, L. Huang, S. Chai, H. Zhai, and J. Zhang, Spin-orbit coupled degenerate Fermi gases, Phys. Rev. Lett. **109**, 095301 (2012).
[63] L. W. Cheuk, A. T. Sommer, Z. Hadzibabic, T. Yefsah, W. S. Bakr, and M. W. Zwierlein, Spin-injection spectroscopy of a spin-orbit coupled Fermi gas, Phys. Rev. Lett. **109**, 095302 (2012).
[64] C. D. Brown, S.-W. Chang, M. N. Schwarz, T.-H. Leung, V. Kozii, A. Avdoshkin, J. E. Moore, and D. Stamper-Kurn, Direct geometric probe of singularities in band structure, Science **377**, 1319 (2022).
[65] Y. Li, W. Han, Z. Meng, W. Yang, C. Chin, and J. Zhang, Observation of quantized vortex in an atomic Bose-Einstein condensate at Dirac point, arXiv:2411.16287.
[66] T. Li, L. Duca, M. Reitter, F. Grusdt, E. Demler, M. Endres, M. Schleier-Smith, I. Bloch, and U. Schneider, Bloch state tomography using Wilson lines, Science **352**, 1094 (2016).
[67] S. L. Campbell, R. B. Hutson, G. E. Marti, A. Goban, N. Darkwah Oppong, R. L. McNally, L. Sonderhouse, J. M. Robinson, W. Zhang, B. J. Bloom, and J. Ye, A Fermi-degenerate three-dimensional optical lattice clock, Science **358**, 90 (2017).
[68] C. Huang, X. Zhang, G. Pan, H. Li, K. Sun, X. Dai, and Z. Y. Meng, Evolution from quantum anomalous Hall insulator to heavy-fermion semimetal in magic-angle twisted bilayer graphene, Phys. Rev. B **109**, 125404 (2024).
[69] C. Chin, R. Grimm, P. Julienne, and E. Tiesinga, Feshbach resonances in ultracold gases, Rev. Mod. Phys. **82**, 1225 (2010).
[70] L. Chomaz, I. Ferrier-Barbut, F. Ferlaino, B. Laburthe-Tolra, B. L. Lev, and T. Pfau, Dipolar physics: a review of experiments with magnetic quantum gases, Rep. Prog. Phys. **86**, 026401 (2023).
[71] P. Schauß, M. Cheneau, M. Endres, T. Fukuhara, S. Hild, A. Omran, T. Pohl, C. Gross, S. Kuhr, and I. Bloch, Observation of spatially ordered structures in a two-dimensional Rydberg gas, Nature (London) **491**, 87 (2012).
[72] C. Meldgin, U. Ray, P. Russ, D. Chen, D. M. Ceperley and B. DeMarco, Probing the Bose glass-superfluid transition using quantum quenches of disorder, Nat. Phys. **12**, 646 (2016).